Imaging the Ionosphere with the Global Positioning System

G. A. Hajj, R. Ibañez-Meier, E. R. Kursinski, and L. J. Romans

Jet Propulsion Laboratory, California Institute of Technology, 4800 Oak Grove Dr., Pasadena, California 91109

ABSTRACT

Observing the Global Positioning System with a satellite in low earth orbit in an occulting geometry provides a powerful means of imaging the ionosphere. Tomographic imaging of the ionosphere from space and ground is examined using singular value decomposition analysis. The resolution and covariance matrices are examined, and simulations are performed that indicate that space data are significantly more effective than ground data in resolving both horizontal and vertical structures. It is shown that narrow vertical structures, such as the E layer, can be probed with occultation data. © 1994 John Wiley & Sons, Inc.

I. INTRODUCTION

When a radio wave travels through the ionosphere, it experiences a group delay and phase advance proportional (to leading order) to the total electron content (TEC) between the transmitter and the receiver [1]. The TEC is defined as the line integral of the ionospheric free electron density between the transmitter and the receiver. Measurements of TEC have been achieved by different techniques with different degrees of accuracy and precision; all of these techniques involve a radio beacon satellite and a receiver. With an array of receivers tracking the same or different satellites, it is possible to obtain a set of intersecting links with a TEC measurement for each link. In such cases we have a situation similar to that of X-ray projections in medical imaging, where the image can be obtained using inversion methods. Unlike medical imaging, however, in ionospheric imaging the geometry of the intersecting links can be quite arbitrary, and therefore in many situations there is insufficient strength to provide a unique inversion. In this case one can only reconstruct a solution that contains characteristics that the data are able to resolve.

The possibility of doing two-dimensional ionospheric tomography has been considered by many authors [2–13]. Work by Raymund et al. [4, 12] and Yeh and Raymund [6] showed the limitation of ionospheric tomography as obtained from ground data alone. This is due to the lack of links that cross the ionosphere in a tangential geometry. These links can only be provided by an occultation geometry, in which a transmitting satellite is setting or rising behind the earth's atmosphere as seen by a receiver in space. This is possible through the use of signals transmitted by satellites of the Global Positioning System (GPS) and received by one or more other satellites in Low Earth Orbit (LEO) (Figure 1).

Received 20 January 1994; revised manuscript received 2 June 1994.

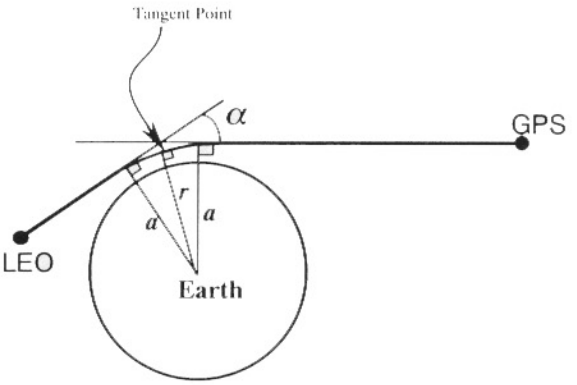

Figure 1. Occultation geometry for GPS and a low earth orbit satellite.

As the signal passes through the ionosphere, its phase speeds up and it bends, in accordance with Snell's law, as a result of the changing index of refraction of the ionosphere. Ignoring bending and other higher-order effects [1], one can find the total electron content along the straight line between the GPS and LEO satellites with a simple linear combination of the dual L-band frequencies of the GPS. (Bending on the day side is of the order of 0.01°; ignoring bending is certainly valid as a first approximation.) Using an onion-shell model for the ionosphere, one can solve for the index of refraction at different layers, as the tangent point (r in Figure 1) starts at the top of the ionosphere and descends into deeper layers of the atmosphere. (For a situation in which the bending cannot be neglected, the Abel transform provides the appropriate formalism in the case of spherical symmetry [14].) With a satellite at 800 km altitude, the ray descends (ascends) for a setting (rising) GPS at a speed of about 3 km/s. This implies that it takes < 5 min to sample the ionosphere in the occultation region. Radio occultation techniques have a heritage of over 20 years in NASA's planetary program [14–16], but the concept, which can be applied to both the neutral atmosphere and the ionosphere, is a newcomer in the earth science arena [17–22].

The GPS consists of 24 satellites in 6 evenly distributed orbital planes, with an inclination of ~55°, altitude ~20,200 km, and a revolution period of ~12 h (Figure 2). Each satellite transmits two carrier frequencies at L-band, L1 and L2 at 19.0 cm and 24.4 cm, respectively. The carrier signals are modulated by a pseudorandom code that allows

CCC 0899-9457/94/020174-11

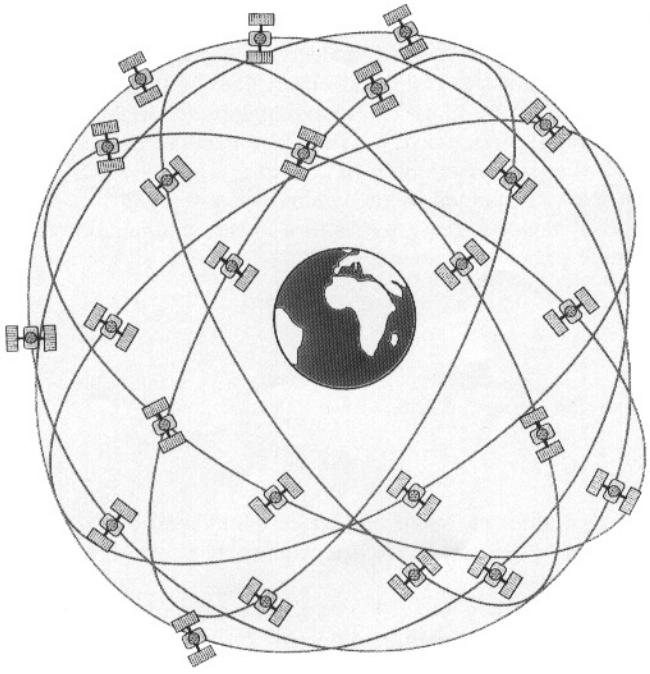

Figure 2. The Global Positioning System constellation.

measuring the absolute time delay between a GPS transmitter and a receiver [23]. This absolute time delay includes the travel time between the transmitter and the receiver, the effect of the medium (which may include the ionosphere and the neutral atmosphere, depending on the location of the receiver), and clock biases of transmitter and receiver in addition to noise. It has been demonstrated that clock biases can be solved for to nanosecond-level accuracies [24]; this implies that absolute TEC measurements from GPS can be obtained with an accuracy of a few TEC units (1 TEC unit = 10^{16} e/m^2). On the other hand, changes in TEC obtained directly from the carrier phase measurements can be as accurate as 0.003 TEC units.

Although the GPS was designed and funded by the U.S. Air Force mainly for the purpose of navigation, the civilian community has taken advantage of its presence for a host of other applications. These include investigation of seismic tectonic motions [25], earth orientation and polar motion studies [26–27], gravimetry [28], atmospheric water vapor and ionospheric calibration [29–30], and ionospheric monitoring [31]. Atmospheric occultation is yet another important application of the GPS in the areas of climate and weather monitoring [17–22]. The idea of using the GPS for the purpose of ionospheric imaging, first suggested by Yunck et al. [32], has been the subject of several studies in the literature [13, 33–35].

In this article, we examine ways by which an LEO satellite tracking GPS can be used to image the ionosphere. We begin be considering the problem of combining links taken from different ground receivers and/or space occultations, to reconstruct horizontal and vertical structures in the ionosphere. As discussed in section II, this is done by working out a two-dimensional example, serving to define the tomographic formalism, and answering basic questions such as the expected resolution and accuracy as a function of the geometry of the transmitting and receiving elements as well as data noise. Within the context of this example, we perform simulations in which a realistic model of the ionosphere is used to generate data and a two-dimensional image is reconstructed tomographically, as discussed in section III. Both of these sections serve to evaluate the relative strengths and weaknesses of ground, space, and combined data sets.

In section IV, we consider means of analyzing individual occultations. By imposing constraints to reduce the tomographic formalism to one dimension, we demonstrate that high resolution vertical profiles of the ionosphere can be obtained. Section IV contains some concluding remarks.

II. TOMOGRAPHIC FORMALISM AND COVARIANCE ANALYSIS

Consider a two-dimensional geometry at a fixed longitude, extending from −50°N to +60°N latitude and from 90–970 km altitude. We divide this region into 44 × 44 pixels, where each pixel will have a height of 20 km and a width of 2.5°. Consider a configuration of seven ground receivers, evenly distributed in latitude between −25°N and +35°N, tracking an LEO satellite passing over the region. In addition, consider a set of seven occultations in the same plane, with tangent points occurring at the same set of latitudes. The geometry is schematically displayed in Figure 3a.

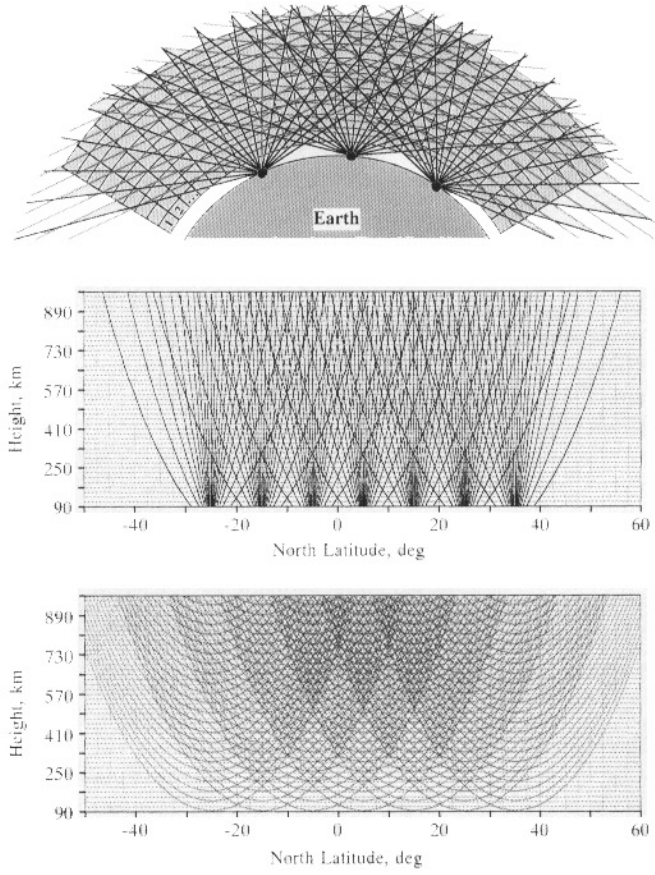

Figure 3. a) (Top panel): Schematic geometry of the ionospheric discretization and the ground and space viewing geometry. b) (Middle panel): Pattern of links from seven ground receivers, against 44 × 44 grid of pixels. c) (Bottom panel): Pattern of links from seven occultations, against 44 × 44 grid of pixels.

The ground and occultation links are shown in spherical coordinates in Figure 3b and c, respectively, against the actual 44×44 set of pixels. The links are geometrically straight lines up to negligible bending effects; the curvature in Figure 3b and c is an artifact of the coordinate system. A cutoff of 10° elevation is applied to the ground measurements. Data below this cutoff are normally susceptible to multipath from the local environment and can be very noisy. Ground and occultation data were taken at regular intervals in space; only every fourth link is shown in Figure 3b and c for clarity.

Let the electron density function be denoted by $f(\underline{r})$ where $\underline{r}$ is a vector from a suitable origin to a given point in the image. A TEC measurement is then given by:

$$C_j = \int_{Raypath\ j} f(\underline{r})\, ds\ ; \quad j = 1,\ no.\ of\ links\ , \tag{1}$$

where ds is an increment along a specific link j. We choose the following basis to span our solution:

$$\begin{aligned} f_i(\underline{r}) &= 1 \quad \text{if} \quad \underline{r} \in \text{pixel } i\ ; \\ &= 0 \text{ otherwise}\ . \end{aligned} \tag{2}$$

We approximate $f(\underline{r})$ by its digitized function, $f_d(\underline{r})$, which is defined by:

$$f_d(\underline{r}) = \sum_i x_i f_i(\underline{r})\ , \tag{3}$$

where x_i is the average of $f(\underline{r})$ in the ith pixel. Equation (1) can then be written in matrix form as:

$$\underset{m \times 1}{C} = \underset{m \times n}{D}\ \underset{n \times 1}{X} + \underset{m \times 1}{E}\ , \tag{4}$$

where C is a column of m measurements, X is a column of the n unknown x_is, E is a column representing the error due to data noise and discretization, D is an $m \times n$ matrix with d_{ji} being the length of link j that lies in pixel i. The variance of an element of E, denoted by σ_j, has two components: the measurement noise and the error introduced by discretization. Given the high precision of TEC measurements obtainable with the GPS system, σ_j is dominated by the latter of these two errors. The discretization error, and hence σ_j, will be a function of the size of the pixel and the variability of the medium. In what follows, we assume $\sigma_j = \sigma$ for all js. The importance of determining σ will become evident subsequently.

In general, the matrix D will not be of full rank; that is, only a subset of the system of m equations (4) will be linearly independent. Moreover, the number of independent equations, L, is in general less than n, the number of unknowns. The result is an underdetermined system of equations, for which singular value decomposition (SVD) of the matrix D allows us to remove the linearly dependent equations [36–39]. Performing the SVD, we write:

$$\underset{m \times n}{D} = \underset{m \times L}{U}\ \underset{L \times L}{W}\ \underset{L \times n}{V^T}\ , \tag{5}$$

where W is a diagonal $L \times L$ matrix with diagonal elements $(w_1, w_2, \ldots, w_L)$, sorted in decreasing order, which correspond to the nonzero singular eigenvalues of D. The columns of U and V are the corresponding left and right singular eigenvectors, respectively. This factorization allows us to break the parameter space of X into two vector spaces. The first space is spanned by the columns of $V = (v_1, v_2, \ldots, v_L)$. A given vector v_i corresponds to a linear combination of the original parameters, namely:

$$x_i^* = \sum_j v_{ij} x_j \tag{6a}$$

which can be solved for, with a variance given by:

$$\sigma_i^{*2} = \sigma^2 / w_i^2\ . \tag{6b}$$

The second space is the null space annihilated by D, corresponding to the region of parameter space to which our data are not sensitive.

The singular values (SVs) of the example of Figure 3 are shown in Figure 4 for three different cases where 1) data from ground alone, 2) data from space alone, and 3) data from ground and space are included. The number of data points in these cases is 567, 616, and 1183, respectively. In case 1, the SVs steadily decline by two orders of magnitude for the first 452 values, after which a sharp cutoff appears. A similar sharp cutoff appears in case 3 beyond approximately the 1050th SV. The largest singular value w_1 corresponds to the best determined linear combination of the parameter space, namely, x_1^* of Equation (6a). The second singular value w_2 corresponds to the second best determined linear combination, and so on. The geometric interpretation of the eigenvectors v_i is that the first vector v_1 is the one that is most nearly parallel to the rows of D; therefore, it is the most nearly parallel to the direction of the links providing the measurements. The second vector is the second most nearly parallel, and so forth [36]. The fact that the SVs of case 2 are larger than those of case 1 reflects the strength of the space data over the ground data.

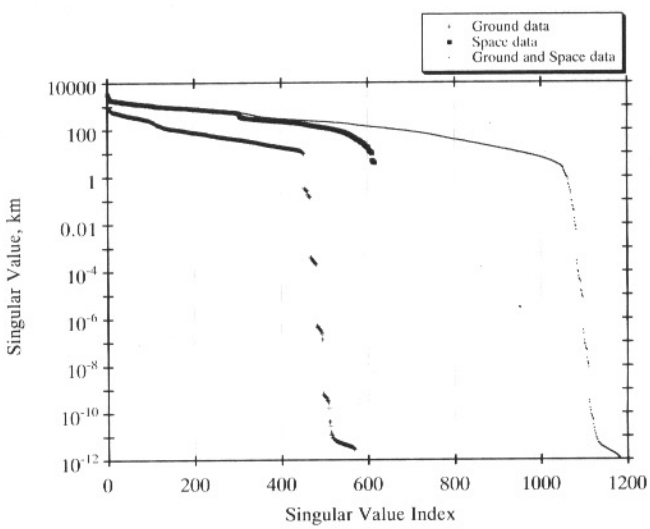

Figure 4. Singular values for three different cases: ground, space, and combined data.

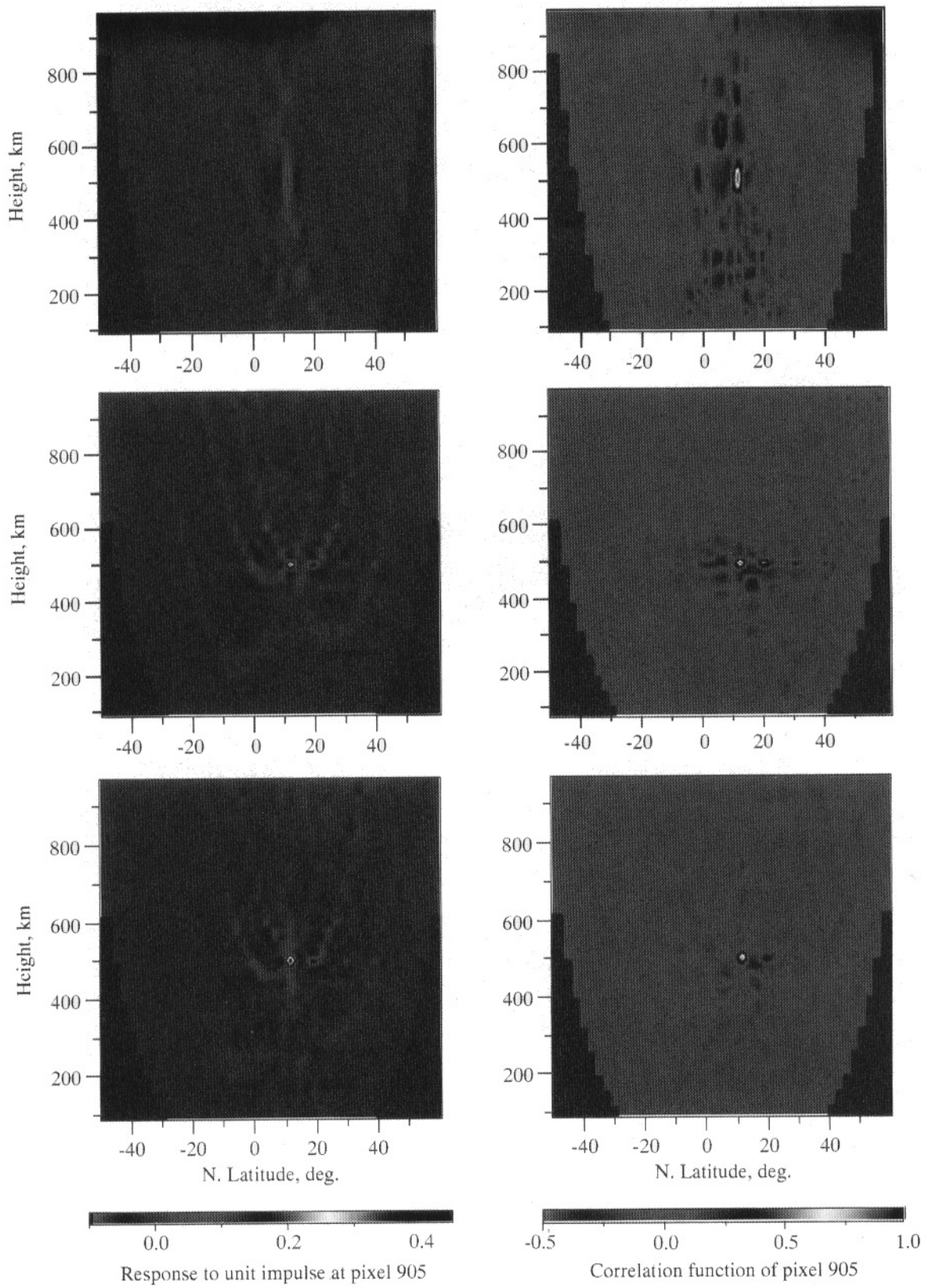

Figure 5. The reconstruction of a unit impulse function (left panels) and the correlation function (right panels) at pixel 905 for the three different cases: ground (top panels), space (middle panels), and combined data (bottom panels). See color plate p. 187.

On the other hand, the first 300 SVs of case 2 and case 3 are nearly identical. The strength gained by adding the ground data to the space data depends on how many SVs are included in the solution, as discussed subsequently.

The least-squares solution for the system is given by:

$$X = VW^{-1}U^{T}C \tag{7}$$

and the solution covariance by:

$$cov(X) = \sigma^{2}VW^{-2}V^{T} \tag{8}$$

The solution given in Equation (7) is undetermined up to an arbitrary linear combination of the vectors spanning the null space. By not including any of these vectors, we are choosing the least norm solution among all possible solutions.

In the presence of some *a priori* knowledge about the ionosphere, one would set up the problem in exactly the same way as before, but now X would correspond to the deviation from the *a priori* nominal values for the electron density in each pixel, and C would be the difference between the measured value and the one calculated based on the *a priori*.

A fundamental issue is to choose the number of nonzero singular values, w_i, to include in our solution. It is important to note from Equation (7) that the more singular values we include in the solution, the closer we get to the true solution. On the other hand, including more and therefore smaller singular values causes the solution covariance to grow very rapidly, as seen from Equation (8). Different methods have been applied in choosing a cutoff value for the number of singular values, to include [36, 37]. The essential point is to choose a cutoff such that the variance associated with the corresponding eigenvectors as given by Equation (6b) makes physical sense. For instance, in the example above, suppose that $\sigma = 10^{16}$ (e/m^2) for the TEC measurement errors. The actual errors are due to data noise and discretization, as explained earlier. Then, an SV cutoff of 100 km would correspond to 10^{11} (e/m^3) of uncertainty in the electron density, according to Equation (6b). Given that the electron density to be recovered can be of the same order of magnitude or smaller, this implies that one should not try to include more singular values in the solution.

Figure 5 shows the response to a unit impulse in pixel 905 (left panels) and the correlation function for that pixel (right panels) for the three cases discussed previously, where ground data (top panels), space data (middle panels), and combined ground and space data (bottom panels) are included. The response to a unit impulse in pixel i is the ith column of the matrix VV^T, and the correlation between pixels i and j is given by $\mathrm{cov}_{ij}/\sqrt{\mathrm{cov}_{ii}\mathrm{cov}_{jj}}$, where the cov matrix is given in Equation (8). In all these cases, only singular values larger than 100 km are included. The brightest spot on the left panels (corresponding to pixel 905) has a peak at 0.13, 0.37, and 0.48 for the three respective cases. The height and width of the unit impulse response are direct measures of the strength of the data. The main features to be seen in Figure 5 are the vertical smearing of the unit impulse response and the correlation function for the ground data, corresponding to the direction of links, and an analogous (though less dominant) horizontal smearing of the unit impulse along the direction of links for the space data (compare the middle left panel of Figure 5 to Figure 3c). The formal errors at pixel 905 (i.e., $\sqrt{\mathrm{cov}_{905,905}}$) are 1.9×10^{10}, 2.1×10^{10}, and 2.6×10^{10} (e/m^3) for the three different cases. These values cannot be directly interpreted as an indication of how well the solution is determined at the given pixel, because of the existence of very high correlations among the pixels.

The formalism in this section is not restricted to a basis consisting of pixels, but can be generalized to any finite set of functions in which one chooses to expand the solution. The major criterion for a given basis is how well it spans actual structures in the ionosphere, because the associated discretization is a major contributor to the size of σ. If the basis functions chosen correspond to the correct modes of the image, then an accurate image can be obtained with a very restricted, but appropriate, set of data. This situation is demonstrated by the work of Raymund et al., in which a set of empirical orthonormal functions is used as a basis to capture large scale features of the ionosphere from a limited set of data [11, 12].

The SVD formalism is particularly appropriate for addressing the interrelationship between the configuration of measurement links, the data noise, and the basis functions; however, SVD does not convey any information on how well a given basis fits the actual image. A simple example will help to illustrate these points. Consider the simple finite two-dimensional image of the ionosphere shown in Figure 6, where the density is constant inside of each pixel. Furthermore, assume that our data are noiseless. Now consider scanning through the image from a specific angle, θ_1, such that each new link encounters one additional new pixel at a time. Then each data point will give the density of the additional new pixel through which it passes. This process will allow us to reconstruct the densities in all the pixels from a single viewing angle of the image. An SVD analysis of links 1–4 yields four nonzero singular values. On the other hand, an SVD analysis of links 5–8 gives only two nonzero singular values, as only two of links 5–8 are independent. In reality, if the picture is not discretized in exactly the same manner in which we chose our pixels here, links 1–4 will not be superior to links 5–8. The SVD can reveal when a set of links is more or less appropriate to a given set of basis functions; however, it cannot tell us

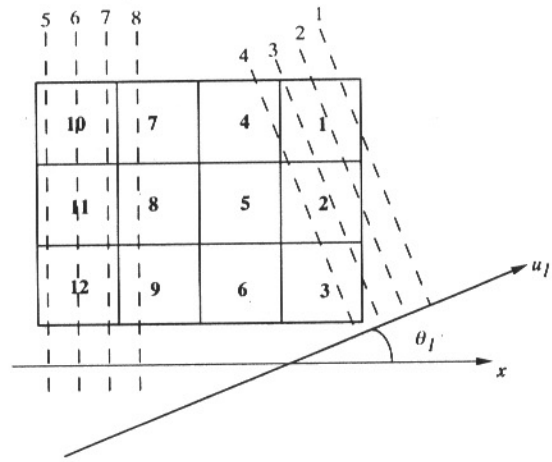

Figure 6. A simple model illustrating the dependence of the data strength on the basis functions.

which set of basis functions best describes, and which set of measurements best probes, the modes of the actual image.

III. TOMOGRAPHIC SIMULATION

In this section we examine the relative strength of ground and space links with a simulation of real data for the examples of section II (Figure 3). The data are generated based on a two-dimensional slice of the ionosphere (top panel of Figure 7), which is created by the Parameterized Ionospheric Model (PIM) [40]. This two-dimensional slice corresponds to the electron density at 20°E geodetic longitude, 12:00 h universal time, September 26, 1992, and extends from −50° to +60°N geodetic latitude. The density is representative of the ionosphere during daytime and solar maximum. The two-dimensional image has a main lobe at about 23°N latitude and 350 km altitude with a peak density of 2.3×10^{12} (e/m^3).

The second panel of Figure 7 shows the reconstruction of the region from ground data alone. The reconstruction smears the image vertically throughout the entire region in a way that all vertical structures of the image are essentially lost. Only horizontal structure, such as the maximum density between 15°N and 30°N, is reflected in the reconstruction. The failure of the ground data alone to capture the vertical structure is due to the strong correlation of the ground data at all elevations with zenith measurements. This correlation makes the D matrix highly singular, and as explained earlier, only linear combinations of electron densities that are mostly parallel to the data links are well determined. This phenomenon is also reflected in the vertical smearing of the unit impulse response and correlation functions displayed in Figure 5 (top panel).

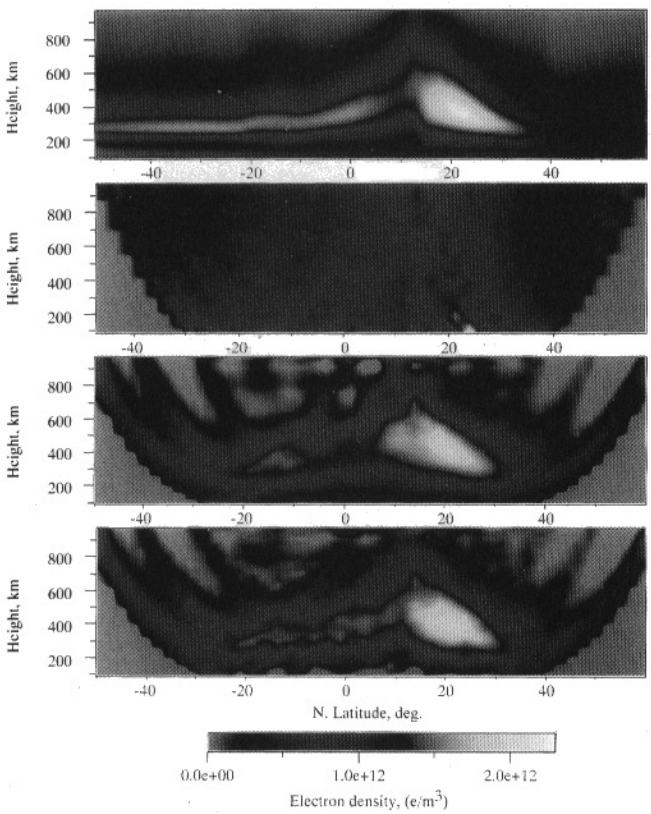

Figure 7. Simulated electron density using the PIM model at 20°E geodetic longitude, at 12:00 h UT (top panel); reconstruction for the three different cases: ground (second panel), space (third panel), and combined data (bottom panel). See color plate p. 187.

The inability to capture vertical structures with ground data alone using conventional tomographic methods or the convolution back projection algorithms is reflected in the literature [4, 7]. More recently, Raymund [11] and Raymund et al. [12] used empirical orthonormal functions as a basis to capture large-scale structures of the ionosphere in both the horizontal and vertical directions. However, in this way only features in the ionosphere that are truly represented by the empirical orthonormal set of functions can be recovered. And even then, as discussed in the pedagogic example at the end of the preceding section, only those functions to which the ground data are sensitive can be solved for.

The third and fourth panels of Figure 7 show the reconstructions of the region from space data alone, and combined space and ground data, respectively. In both of these cases, we start to distinguish some of the more detailed features of the two-dimensional structure, such as the high electron density near 20°N latitude and 300–400 km altitude. The general shape of the main lobe in the true image is also reflected in the reconstructions. The maximum reconstructed electron density in these two cases are 2.07×10^{12} and 2.14×10^{12} (e/m^3). The inclusion of ground data helps in resolving some of the finer details of the image, such as the narrow strip of electron density at ~300 km, extending from −50° to 10°N latitude. The advantage of the space data over the ground data in simultaneously resolving both vertical and horizontal structure is apparent from the way the links cross each other at a wider range of angles (compare Figure 3b and c).

In the three cases discussed above, the smallest singular value included in the solution was equal to 100 km. The fact that the solutions are of minimum norm, with no assumed *a priori*, explains why the true density is underestimated. Furthermore, no constraints were applied, which resulted in some negative electron densities. The results could be improved by imposing a positivity constraint.

The examples considered here provide an indication of the relative strength of space and ground data. In a real-life situation, one would not expect extended sequences of nearly coplanar space occultations, unless there were a set of LEO satellites closely following each other in the same orbital plane. (In fact, this possibility might be realized; constellations of tens or even hundreds of communication satellites in LEO bearing GPS receivers are under consideration.) However, the presence of just a few satellites in LEO tracking the GPS will provide a fairly dense coverage for the reconstruction of three-dimensional tomographic images. Even when occultations are too sparse for a full tomographic inversion, individual occultations can be analyzed by imposing constraints (e.g., spherical symmetry) so that the tomographic approach collapses into a one-dimensional problem. This topic will be discussed in the next section.

IV. ANALYSIS OF INDIVIDUAL IONOSPHERIC OCCULTATIONS

With the full constellation of the GPS satellites, a single GPS receiver in a near polar orbit will observe over 500 occulta-

tions per day, spread about the globe. The first set of earth ionospheric occultations using GPS will become available with the launch of GPS-MET, scheduled for September 1994. GPS-MET will be placed at 800 km altitude with a high precision receiver, capable of tracking up to eight GPS satellites simultaneously. With an aft-looking antenna, the GPS-MET will cover half of the full sky and therefore provide over 200 globally distributed occultations daily. Figure 8 shows representative coverage of the GPS-MET during one day.

In the previous two sections, space and ground data were used in the context of tomography, where both horizontal and vertical structure are solved for simultaneously. However, when occultations are too sparse to allow a tomographic inversion, extra constraints can be applied to reduce the dimensionality of the problem. The data from an individual occultation are generally sufficient to invert a one-dimensional problem. For instance, one can assume spherical symmetry and solve for a vertical profile with very high resolution, as will be shown subsequently.

The theoretical limit of the vertical resolution obtainable in a limb geometry is set by the diffraction limit of the geometric optics approximation, in which the vertical and the cross-beam dimensions of the sampling volume are given by the diameter of the first Fresnel zone. In the absence of bending, the first Fresnel zone is approximately given by the diameter of a cone with its apex at the receiver, its axis defined by the line from the receiver to the tangent point, and the rays forming the cone having length given by this distance plus one-half the radio wavelength. The Fresnel zone corresponds to about 1 km for GPS-MET observing a GPS satellite in a limb geometry. However, a more serious limitation in reconstructing accurate ionospheric vertical profiles of electron density from occultation data alone is due to the relatively large horizontal structure that the signal has to probe, causing the spherical symmetry assumption to be rendered inaccurate. In what follows, we will examine how well one can do by ignoring the horizontal gradient, and means of improving that approach.

We use our simulated structure of Figure 7 (top panel) as the truth. To examine the effect of the ionosphere on the signal, we assume a configuration whereby an LEO satellite and a GPS are in an occultation geometry, with the tangent point of the occultation link at 20°N latitude. This latitude corresponds to the region of maximum electron density profile in our two-dimensional grid. The amount of bending and signal delay as functions of the height of the tangent point is shown in Figure 9 for the GPS L1 signal. (The effect on the L2 signal is the same but a factor of 1.65 larger.) The negative delay implies a phase advance. The curvature at a given point on the LEO-GPS ray is in the direction of increasing index of refraction (i.e., decreasing electron density). A positive sign of the bending angle is such that the curvature of the ray is toward the center of the earth. The bending of the ray is directly proportional to the amount of Doppler shift that the ray experiences, which is in turn proportional to the phase rate of change. This explains why the bending changes sign at the point where the delay has its maximum magnitude, near the F2 peak. The oscillations in bending near the E region are, similarly, due to the change in curvature of the delay. It is worth noticing that even during the daytime and near solar maximum, the absolute bending does not exceed 0.016° (0.026) for L1 (L2). The magnitude of the delay for L1 is about 90 m, which corresponds to a total electron content of about 250×10^{16} e/m^2.

Given that the bending is small, in the following analysis we will assume that the signal travels along a straight path connecting the transmitter and the receiver. Assuming a locally spherically symmetric ionosphere, we solve for the electron density profiles for several occultations with tangent points at −20°, 0°, 20°, and 40°N geodetic latitude. Figure 10 shows the true electron density (solid line) and the reconstruction (open diamond) at these latitudes. The two peaks of each profile correspond to the F2 peak at 300–400 km altitude and the E peak at ~100 km altitude.

The following observations will help in understanding some of the effect of the spherical symmetry assumption on the reconstruction. The solution at 20° latitude largely underestimates the true profile. The true electron density profile at about 20° corresponds to a maximum in the plane of occultation. This implies that the signal would be slower on both

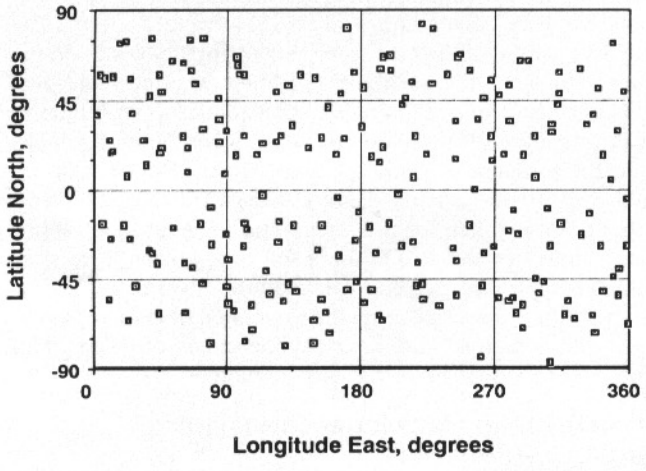

Figure 8. A representative daily occultation coverage for GPS-MET (total of 219 occultations).

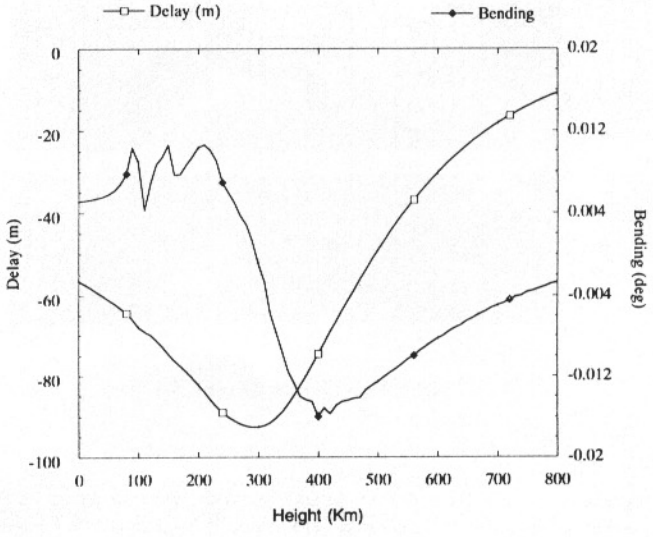

Figure 9. Delay and bending of the GPS L1 signal as it traverses the earth's ionosphere.

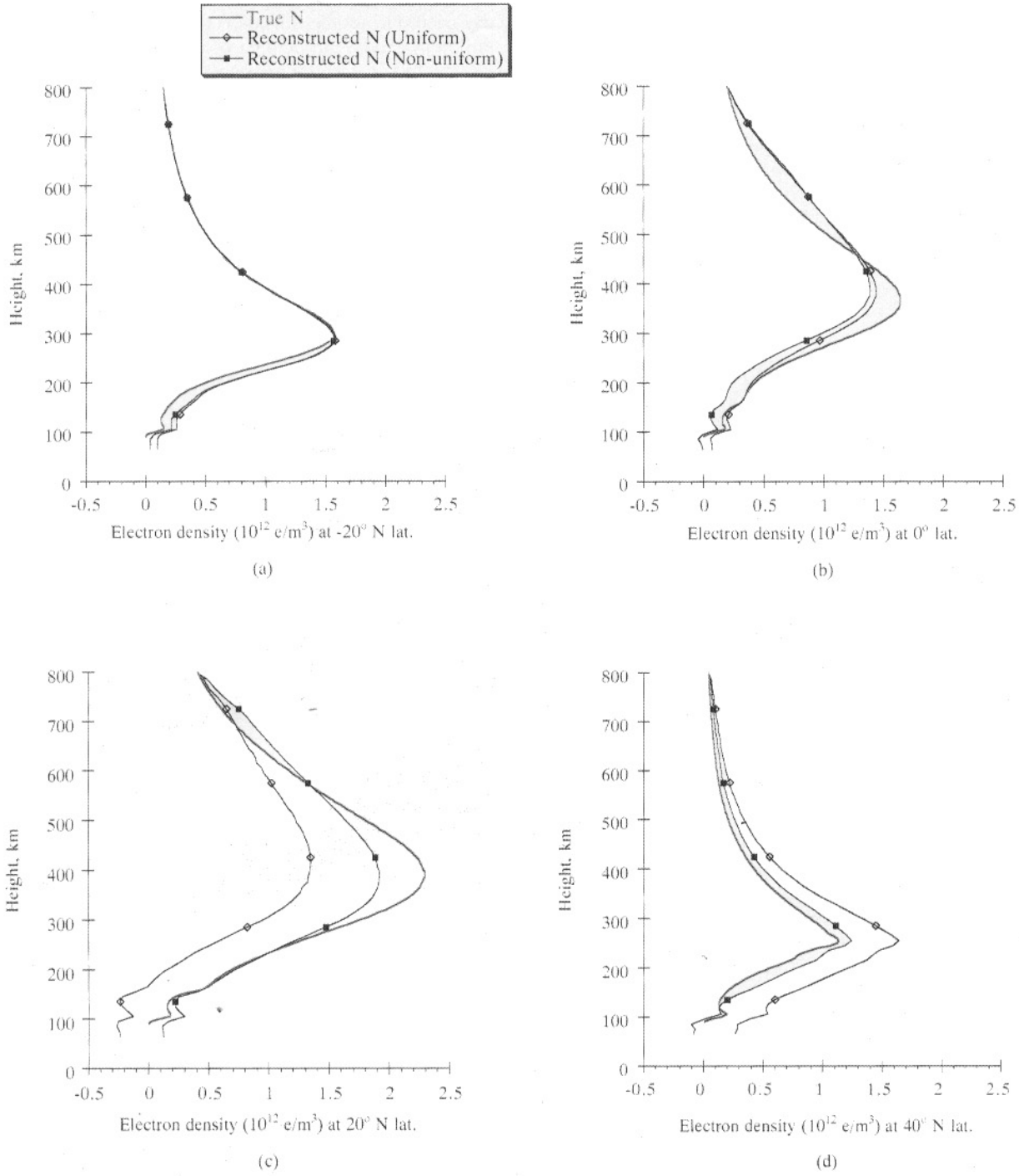

Figure 10. Vertical slices of the two-dimensional image of the top panel of Figure 7 at a) −20°, b) 0°, c) 20°, and d) 40°N latitude, showing truth (solid line) versus reconstructed assuming spherical symmetry (open diamond), and reconstructed assuming specified horizontal gradient (solid square).

sides of the tangent point; therefore, on average, it would give a smaller estimate of the electron density. However, under general conditions, when the profile corresponds to neither a maximum nor a minimum with respect to its surrounding area, a cancellation effect takes place and a more accurate reconstruction can be obtained. For instance, if for each layer through which the signal is passing we have an index of refraction that is changing linearly as a function of the arc length from the tangent point of occultation, the signal slows down and speeds up around the tangent point by exactly the same amount, so that the estimated refractivity is exactly that of the tangent point. In general, all odd components of the horizontal gradient around the tangent point cancel; only even terms contribute to the error in refractivity [20]. This explains the almost exact agreement between the reconstructed and the true profile above the F region for the −20° latitude case,

where the actual electron density at that latitude is not exactly spherical. On the other hand, a sharp horizontal gradient in the electron density appears between 20–40° latitude and the gradient gets considerably smaller beyond 40°. The net effect on the occultation with a tangent point at 40° is that the signal will travel faster on one side of the tangent point, but not slow enough on the other side to compensate for the increase in the first side, resulting in an overestimate of the electron density.

Another problem of the reconstructed profile is that it depicts a negative electron density at the bottom of the ionosphere, which is a physical impossibility. Imposing positivity on the solution can be used as an extra constraint to improve the results.

A first order improvement over the spherically symmetric assumption is to divide the ionosphere into pixels in the same manner that was done for the tomography of section III, then constrain pixels lying next to each other horizontally (i.e., in the same layer) to have a given functional form with an undetermined scale factor. This functional form can be the same for all layers, or different for different layers. The problem is then reduced to solving for the single unknown scale factor for each layer, reducing a two- or three-dimensional problem to a one-dimensional problem. This can be explicitly formulated as follows. Consider Equation (4), where X is the column of n unknown densities corresponding to n pixels. Suppose we have a two-dimensional image that is divided in polar coordinates into Q slices in the angular direction and P layers radially. Let r_i be the radius of layer i and θ_j be the angle of the center of slice j. We correlate the elements of X as follows:

$$\begin{aligned}
x_1 &= a_1 g(r_1, \theta_1) \\
x_2 &= a_1 g(r_1, \theta_2) \\
&\vdots \\
x_Q &= a_1 g(r_1, \theta_Q) \\
x_{Q+1} &= a_2 g(r_2, \theta_1) \\
&\vdots \\
x_{2Q} &= a_2 g(r_2, \theta_Q) \\
x_{2Q+1} &= a_3 g(r_3, \theta_1) \\
&\vdots
\end{aligned} \tag{9}$$

where $a_1, a_2, \ldots$ are unknown scaling factors and $g(r, \theta)$ is a given *a priori* function. Then Equation (4) reduces to:

$$\underset{m\times 1}{C} = \underset{m\times P}{B}\ \underset{P\times 1}{A} + \underset{m\times 1}{E} \tag{10}$$

where $A^T = (a_1, a_2, \ldots, a_P)$ and the elements of B are given by:

$$\begin{aligned}
B_{1,1} &= d_{1,1} g(r_1, \theta_1) + d_{1,2} g(r_1, \theta_2) + \cdots + d_{1,Q} g(r_1, \theta_Q) \\
B_{1,2} &= d_{1,Q+1} g(r_2, \theta_1) + d_{1,Q+2} g(r_2, \theta_2) + \cdots \\
&\quad + d_{1,2Q} g(r_2, \theta_Q) \\
&\vdots
\end{aligned} \tag{11}$$

d_{ij} are the original elements of the matrix D in Equation (4). By introducing the function $g(r, \theta)$ relating the values at different pixels, the number of unknowns is reduced to P. In the case of an occultation, one can choose $m = P$ independent measurements and, therefore, obtain a unique solution for A^T.

Figure 10 shows the reconstructed profiles when the same functional form is applied to all the layers of the ionosphere, namely $g(r, \theta) = g(\theta)$. The applied function $g(\theta)$ is taken to correspond to the zenith total electron content from the ground up to 1000 km height at the given latitude θ. Such data are generally available from models, or from global zenith TEC maps generated using GPS, or other empirical means [30, 34]. With the application of the same horizontal gradient to correlate pixels at a given layer, the solution improves on the average, as seen from Figure 10 (solid squares). Further improvement is still possible by applying different horizontal gradients to the different layers, as can be obtained from tomographic analyses, interpolation of nearby occultations, or models.

One of the most striking characteristics of all the reconstructed profiles of Figure 10 is that the data are sensitive to the E layer of the ionosphere. Even when the simplest approach is being used, namely when spherical symmetry is assumed, the point-to-point structure of the E layer is recovered, but the overall level is off. By constraining the solution to fall within lower and upper bounds at certain heights, the overall level can be improved. GPS provides a unique system for sensing the E layer of the ionosphere, which, under normal conditions, cannot be detected from ground data alone.

V. CONCLUSION

The work discussed in this article suggests that data from space are sufficient in themselves to provide considerable information on the large-scale horizontal and vertical structure of the ionosphere. On the other hand, ground data can provide detailed information on horizontal structure, but are of extremely restricted utility in sensing vertical structures. In the analysis of a single space occultation, where the GPS-LEO data are insensitive to the horizontal structure, ground data can be used to constrain the form of horizontal variation, resulting in significant improvements to the profile solutions. The GPS-LEO data are sensitive to small vertical structures in the ionosphere such as the E layer.

Generally speaking, when tomography is employed to reconstruct the ionosphere, one cannot expect sufficient strength in the data to obtain a unique solution. Resolution and accuracy are very much dependent on the model used, the variability of the medium, and the data noise. The importance of choosing the proper basis to expand a solution has been demonstrated in the ionospheric tomography literature [11, 12]. Singular value decomposition can be very useful in determining what linear combinations of the basis functions the data can resolve and to what accuracy. SVD is also a natural utility to examine questions of model and data resolution.

There are several natural directions in which the work described here can be extended. It would be interesting to investigate a fully three-dimensional tomographic reconstruction of the ionosphere with a realistic set of occultations. Another area that deserves further study is to investigate the

value of using profiles obtained from space as *a priori* information for ground-based tomography.

ACKNOWLEDGMENTS

The work described here was carried out at the Jet Propulsion Laboratory, California Institute of Technology, under contract with the National Aeronautics and Space Administration.

REFERENCES

1. S. Bassiri and G. A. Hajj. "Higher-order ionospheric effects on the Global Positioning System observables and means of modeling them," *Manuscripta Geodaetica* **18**, 280–289 (1993).
2. J. R. Austen, S. J. Franke, and C. H. Liu. "Ionospheric imaging using computerized tomography," *Radio Sci.* **23**, 299–307 (1988).
3. H. Na and H. Lee. "Resolution analysis of tomographic reconstruction of electron density profiles in the ionosphere," *Int. J. Imaging Syst. Technol.* **2**, 209–218 (1990).
4. T. D. Raymund, J. R. Austen, S. J. Franke, C. H. Liu, J. A. Klobuchar, and J. Stalker. "Application of computerized tomography to the investigation of ionospheric structures," *Radio Sci.* **25**, 771–789 (1990).
5. H. Na and H. Lee. "Orthogonal decomposition technique for ionospheric tomography," *Int. J. Imaging Syst. Technol.* **3**, 354–365 (1991).
6. K. C. Yeh and T. D. Raymund. "Limitations of ionospheric imaging by tomography," *Radio Sci.* **26**, 1361–1380 (1991).
7. H. Na. *Tomographic Reconstruction Techniques for Imaging Electron Density Profiles in the Ionosphere*, Ph.D. thesis, University of Illinois at Urbana-Champaign, Urbana, Illinois, 1991.
8. D. J. Fremouw, J. A. Secan, and B. M. Howe. "Application of stochastic inverse theory to ionospheric tomography," *Radio Sci.* **27**, 721–732 (1992).
9. V. E. Kunitsyn and E. D. Tereshchenko. "Determination of the turbulent spectrum in the ionosphere by a tomographic method," *J. Atmos. Terr. Phys.* **54**, 1275–1282 (1992).
10. T. D. Raymund, S. E. Pryse, L. Kersley, and J. A. T. Heaton. "Tomographic reconstruction of the ionospheric electron density with European incoherent scatter radar verification," *Radio Sci.* **28**, 811–817 (1993).
11. T. D. Raymund. *Development and Applications of Ionospheric Tomography*, Ph.D. thesis, University of Illinois at Urbana-Champaign, Urbana, Illinois, 1993.
12. T. D. Raymund, S. J. Franke, and K. C. Yeh. "Ionospheric tomography: Its limitations and reconstruction methods," *J. Atmos. Terr. Phys.*, in press.
13. G. A. Hajj, R. Ibañez-Meier, and E. R. Kursinski. "Ionospheric imaging from a low earth orbiter tracking GPS," in Proceedings of the ION-GPS 93 Conference, Institute of Navigation, Salt Lake City, Utah, 1993, pp 1315–1322.
14. G. Fjeldbo, A. J. Kliore, and V. R. Eshleman. "The neutral atmosphere of Venus as studied with the Mariner V radio occultation experiments," *Astronom. J.* **76**, 123–140 (1971).
15. G. L. Tyler. "Radio propagation experiments in the outer solar systems with Voyager," *Proc. IEEE* **75**, 1404–1431 (1987), and references within.
16. M. K. Bird, S. W. Asmar, J. P. Brenkle, P. Edenhofer, O. Funke, M. Patzoid, and H. Volland. "Ulysses radio occultation observations of the Io plasma torus during the Jupiter encounter," *Science* **257**, 1531–1535 (1992).
17. K. R. Hardy, D. P. Hinson, G. L. Tyler, and E. R. Kursinski. "Atmospheric profiles from active space-based radio measurements, in Proceedings of the 6th Conference on Satellite Meteorology and Oceanography, American Meteorological Society, Boston, 1992.
18. K. R. Hardy, G. A. Hajj, and E. R. Kursinski. "Accuracies of atmospheric profiles obtained from GPS occultations," in Proceedings of the ION-GPS 93 Conference, Institute of Navigation, Salt Lake City, Utah, 1993, pp 1545–1557.
19. E. R. Kursinski, G. A. Hajj, and K. R. Hardy. "Temperature or moisture profiles from radio occultation measurements," in Proceedings of the 8th Symposium on Meteorological Observations and Instrumentation, American Meteorological Society, Anaheim, California, 1993, pp J153–J158.
20. E. R. Kursinski, G. A. Hajj, and K. R. Hardy. "Atmospheric profiles from radio occultation measurements of GPS satellites," in Proceedings of the International Society for Optical Engineering Symposium on Optical Engineering and Photonics in Aerospace Science and Sensing, International Society for Optical Eng., Orlando, 1993, paper 1935-13.
21. L. L. Yuan, R. A. Anthes, R. H. Ware, C. Rocken, W. D. Bonner, M. G. Bevis, and S. Businger. "Sensing climate change using the Global Positioning System," *J. Geophys. Res.* **98**, 14925–14937 (1993).
22. G. A. Hajj, E. R. Kursinski, W. I. Bertiger, and L. J. Romans. "Assessment of GPS occultations for atmospheric profiling," in Proceedings of the 7th Conference on Satellite Meteorology and Oceanography, American Meteorological Society, Monterey, California, 1994, paper J4.9.
23. J. J. Spilker. "GPS signal structure and performance characteristics," *Navigation* **25**, 29–54 (1978).
24. B. D. Wilson and A. J. Mannucci. "Instrumental biases in ionospheric measurements derived from GPS data," in Proceedings of the ION-GPS 93 Conference, Institute of Navigation, Salt Lake City, Utah, 1993, pp 1343–1351.
25. G. Blewitt, M. B. Heflin, K. J. Hurst, D. C. Jefferson, F. H. Webb, and J. F. Zumberge. "Absolute far-field displacements from the 28 June 1992 Landers earthquake sequence," *Nature* **361**, 340–342 (1993).
26. A. P. Freeman. "Measuring earth orientation with global positioning system," *Bull. Geod.* **65**, 53–65 (1991).
27. R. P. Malla, S. C. Wu, and S. M. Lichten. "Geocenter location and variations in earth orientation using global positioning system measurements," *J. Geophys. Res.* **98**, 4611–4617 (1993).
28. W. I. Bertiger, J. T. Wu, and S. C. Wu. "Gravity field improvement using GPS data from Topex/Poseidon: A covariance analysis," *J. Geophys. Res.* **97**, 1965–1971 (1992).
29. D. M. Tralli and S. M. Lichten. "Comparison of Kalman filter estimates of zenith atmospheric path delays using the Global Positioning System and very long baseline interferometry," *Radio Sci.* **27**, 999–1007 (1992).
30. B. D. Wilson, A. J. Mannucci, and T. Roth. "Global ionospheric maps using a global network of GPS receivers," in Proceedings of the International Beacon Satellite Symposium, M. C. Lee, Ed., Plasma Fusion Center, Massachusetts Institute of Technology, Beacon Satellite Symposium, 1992, pp 144–147.
31. D. Coco. "GPS-Satellites of opportunity for ionospheric monitoring," *GPS World*, **Oct**, 47–50 (1991).
32. T. P. Yunck, G. F. Lindal, and C. H. Liu. "The role of GPS in precise earth observation," in Proceedings of the IEEE Position Location and Navigation Symposium, Orlando, Florida, 1988.
33. Y. T. Chiu, R. M. Robinson, and G. T. Davidson. "Global 3-d monitoring of the ionosphere with space-based GPS receivers," in Proceedings of the International Beacon Satellite Symposium, M. C. Lee, Ed., Plasma Fusion Center, Massachusetts Institute of Technology, Beacon Satellite Symposium , 1992, pp 148–151.
34. A. J. Mannucci, B. D. Wilson, and C. D. Edwards. "A new method for monitoring the earth's ionospheric total electron content using the GPS global network," in Proceedings of the ION-GPS 93 Conference, Institute of Navigation, Salt Lake City, Utah, 1993, pp 1323–1332.
35. B. D. Wilson, A. J. Mannucci, and C. D. Edwards. "Sub-daily northern hemisphere ionospheric maps using the IGS GPS network," in Proceedings of the 7th International Ionospheric Effects Symposium, J. Goodman, Ed., Alexandria, Virginia, 1993.

36. R. A. Wiggins. "The general linear inverse problem: Implication of surface waves and free oscillations for earth structure," *Rev. Geophys. Space Phys.* **10**, 251–285 (1972).
37. C. L. Lawson and R. J. Hanson, *Solving Least Squares Problems*, Prentice-Hall, Englewood Cliffs, New Jersey, 1974.
38. K. Aki and P. G. Richards, *Quantitative Seismology, Theory and Methods, Vol. II*, W. H. Freeman, San Francisco, 1990.
39. W. Menke, *Geophysical Data Analysis: Discrete Inverse Theory*, Academic Press, New York, 1989.
40. D. N. Anderson, "The development of global, semi-empirical ionospheric specification models," in Proceedings of the 7th International Ionospheric Effects Symposium, J. Goodman, Ed., Alexandria, Virginia, 1993.